

# Geodynamo $\alpha$ -effect derived from box simulations of rotating magnetoconvection

A. Giesecke, U. Ziegler, and G. Rüdiger

*Astrophysikalisches Institut Potsdam, An der Sternwarte 16, D-14482 Potsdam, Germany*

---

## Abstract

The equations for compressible rotating magnetoconvection are numerically solved in a Cartesian box assuming conditions roughly suitable for the geodynamo. The mean electromotive force describing the generation of mean magnetic flux by convective turbulence in the rotating fluid is directly calculated from the simulations and the corresponding  $\alpha$ -coefficients are derived. Due to the very weak density stratification, the  $\alpha$ -effect changes its sign in the middle of the box. It is positive at the top and negative at the bottom of the convective instable layer. For strong magnetic fields we also find a clear downward advection of the mean magnetic field. Finally the quenching behavior of the  $\alpha$ -effect in dependence of the imposed magnetic field strength is presented.

*Key words:* magnetoconvection, geodynamo,  $\alpha$ -effect

---

## 1 Introduction

Convective motions in the fluid outer core influenced by rotation and magnetic fields are able to maintain the Earth's magnetic field for long times interrupted by occasional reversals of the dominating dipole component. The equations describing the physical processes in the fluid outer part of the Earth's core show a broad range of timescales on which the characteristic behavior is observable. The resulting and dominating advective timescale  $\tau_{\text{adv}} = d/u'$  leads to a very short coherence length of the physical quantities like velocity or magnetic field which, as a consequence, requires a very high spatial resolution in numerical simulations in order to include the effects of small-scale turbulence (Hollerbach, 2003). In case of a conducting and rotating fluid with large-scale density stratification, a convective driven turbulence can generate a mean electromotive force (EMF) parallel to the mean magnetic field – a process known as  $\alpha$ -effect (Krause and Rädler, 1980).

Present date 3D hydromagnetic simulations do not consider this term on the grounds that induction on small scales may not be important for the dynamo process. Instead, Roberts and Glatzmaier (2000) explained dynamo-action through the twisting and stretching of magnetic field lines by some kind of large scale  $\alpha$ -effect. For strongly driven (or weakly diffusive) dynamos they obtained solutions of  $\alpha\Omega$ -type where the toroidal field component is produced from the poloidal field by strong shear flows that are caused by thermal winds and/or super-rotation of the inner core. For weakly driven flow Olson et al. (1999) obtained  $\alpha^2$ -dynamos. In both cases the poloidal field is produced from the toroidal field by (anti-)cyclonic fluid motions from Taylor cells outside the tangent cylinder. Drift motions along these column-like structures twist the toroidal magnetic field which finally leads to an average poloidal field component.

In the above mentioned cases the  $\alpha$ -effect operates on a large scale and is different from the mechanism described by Krause and Rädler (1980). The scale on which such  $\alpha$ -effect occurs is uncertain and should strongly depend on the behavior of the small scale turbulence and therefore on the resolvable structures respective on the parameters that could be reached in a geodynamo simulation. To include the effects of small scale turbulence, subgrid scale (SGS) models have been developed that consider the influence of unresolved scales. Buffett (2003) showed that a SGS model based on the self-similarity of the turbulence is able to match amplitude and spatial distribution of the subgrid scale heat and momentum fluxes including anisotropy induced by rotation and the magnetic field. But he did not examine expressions for the subgrid scale Lorentz force and induction because in his simulations the local magnetic Reynolds number  $Rm = u'\delta/\eta$  (where  $\delta$  is the grid resolution) is much smaller than 1 and therefore these scales do not contribute to dynamo action.

Further complications appear through the small value of the molecular magnetic Prandtl number ( $Pm = \nu/\eta \sim 10^{-6}$ ) which suggest a large difference on the scales of turbulence of the fluid motions and the magnetic field. The effective (turbulent) Prandtl number probably is much larger but how to model this quantity is uncertain. Therefore, the size of the smallest scales of turbulent motions (respective the local magnetic Reynolds number) and the corresponding influence on the large scale induction still remains unknown. Full 3D simulations of the MHD-equations with at least a resolution that resolves scales with a local Reynolds number  $\lesssim 1$  are necessary in any case. This requires a huge amount of computer power and limits the length of a simulation run (SGS models even enlarge this requirement). In order to examine the meaning of the small scales for the induction process on the one hand and to get a background for simplifying mean field models on the other, calculation of a geodynamo  $\alpha$ -effect in the sense of the mean-field theory is of interest.

Mean-field models are computationally affordable and therefore are able to

investigate the large scale behavior of the magnetic field on long time scales, of course, with a lack of details and accuracy. Using an  $\alpha\Omega$ -dynamo, Schmitt et al. (2001) analyzed the behavior of a mean-field model which produces an axial dipole with irregularly occurring reversals that are induced by a fluctuating  $\alpha$ . They obtained a connection between the reversal rate of the fundamental dipole mode and the (forcing) parameter that describes the correlation length and -time as well as the amplitude of the  $\alpha$ -fluctuations. Stefani and Gerbeth (2004) presented an  $\alpha^2$ -dynamo model with a spherical symmetric  $\alpha$ -effect that also exhibits polarity changes due to a fluctuating  $\alpha$ -coefficient and retrieved basic properties of geomagnetic reversals. One weakness of their model is the applied radial  $\alpha$ -profile that was taken from calculations done by Stefani and Gerbeth (2003). They determined a radial profile of a spherically symmetric and isotropic  $\alpha$  under the conditions that the dynamo mode with the lowest eigenvalue is an oscillating solution and all stationary modes (that usually dominate  $\alpha^2$ -models) are damped. This constraint leads to an  $\alpha$ -effect with characteristic zeros in the radial profile but the properties of this  $\alpha$  are not justified by any (geo-)physical considerations.

The purpose of the present paper is to find a firmer foundation for such  $\alpha^2$ -mean-field models for the geodynamo as the characteristics of the  $\alpha$ -tensor for the Earth's case are computed. For that the turbulent EMF is calculated directly from numerical solutions of the full set of nonlinear MHD-equations for a convective driven turbulent flow under the influence of rotation and subject to an imposed magnetic field. In principle, the results include effects of anisotropy of the  $\alpha$ -effect, its radial dependence and its quenching properties. A simplified geometry of a Cartesian box that represents a small part of a rotating spherical shell provides the ability to examine the small-scale behavior of the fluid motions and magnetic field. Such a simplified plane-layer model can only serve as a toy model for the conditions in the outer core. Important large scale features, for example the column-like orientation of the flow parallel to the rotation axis (Busse, 1970) and therefore the corresponding large scale induction effects, are ignored. In this sense the box model only roughly resembles the important conditions in the Earth's fluid outer core that are determined by turbulent convection with unstable weak density stratification and fast rotation.

## 2 The model

### 2.1 General properties

Our model is an adaption of configurations used, for example, by Ossendrijver et al. (2001) and Ziegler (2002) who examined rotating magnetoconvection in

a box suitable for the solar convection zone. Figure 1 shows a sketch of the box placed somewhere on a spherical shell at latitude  $\theta$ . The coordinate system is chosen such that the unit vectors  $\hat{x}$ ,  $\hat{y}$ ,  $\hat{z}$  form a right-handed co-rotating system with  $\hat{x}$  pointing towards the equator,  $\hat{y}$  pointing in the toroidal direction (from west to east) and  $\hat{z}$  pointing from the bottom to the top of the box. Translating this Cartesian system into global spherical coordinates,  $\hat{z}$  represents the radial direction  $\hat{r}$  directed from inside to outside,  $\hat{y}$  the azimuthal direction  $\hat{\phi}$  and  $\hat{x}$  the meridional direction  $\hat{\theta}$ , respectively. The angular velocity  $\boldsymbol{\Omega}$  in the co-rotating local box coordinate system is then given by  $\boldsymbol{\Omega} = -\Omega_0 \sin \theta \hat{x} + \Omega_0 \cos \theta \hat{z}$  where  $\Omega_0$  is the angular velocity of the rotating spherical shell.

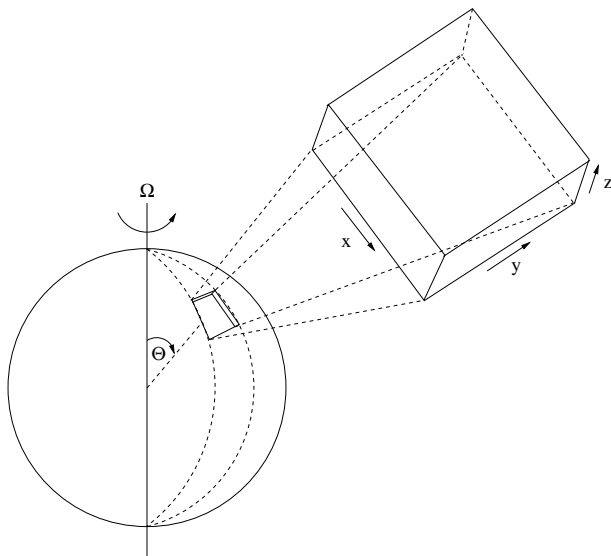


Fig. 1. Model box as part of a rotating spherical shell at latitude  $\theta$ .

To investigate the transition from the weak field case to the strong field case the strength of an imposed magnetic field is successively increased covering a wide range of magnitudes. The principle interest lies on the presence of strong magnetic fields with significant dynamical influence on the flow. In the strong field case this configuration ensures that the inertial and viscous forces are negligible and the main balance between the forces governing the magnetoconvection state is given by the Coriolis force and the Lorentz force as expected in the fluid outer core (Hollerbach, 1996).

Simulations have been performed at a co-latitude of  $\theta = 45^\circ$ . To compute the  $\alpha$ -coefficients several runs are needed where the magnetic field is imposed in different orthogonal directions  $(x, y)$ . The EMF and the mean magnetic fields are directly calculated from the simulations and by combining these results the components  $\alpha_{ij}$  are determined.

## 2.2 Equations

The MHD-equations for a rotating fluid, including the effects of thermal conduction, compressibility, viscous friction and losses due to magnetic diffusivity, are solved numerically using the code NIRVANA (Ziegler, 1998, 1999). The equations in the local co-rotating system are

$$\partial_t \rho = -\nabla \cdot (\rho \mathbf{u}), \quad (1)$$

$$\partial_t (\rho \mathbf{u}) = -\nabla \cdot (\rho \mathbf{u} \mathbf{u}) - \nabla p + \nabla \cdot \sigma + \rho \mathbf{g} - 2\rho \boldsymbol{\Omega} \times \mathbf{u} + \frac{1}{\mu_0} (\nabla \times \mathbf{B}) \times \mathbf{B}, \quad (2)$$

$$\partial_t e = -\nabla \cdot (e \mathbf{u}) - p \nabla \cdot \mathbf{u} + \sigma \cdot \nabla \mathbf{u} + \frac{\eta}{\mu_0} |\nabla \times \mathbf{B}|^2 + \nabla \cdot (\chi \nabla T), \quad (3)$$

$$\partial_t \mathbf{B} = \nabla \times (\mathbf{u} \times \mathbf{B} - \eta \nabla \times \mathbf{B}), \quad (4)$$

with the density  $\rho$ , velocity  $\mathbf{u}$ , pressure  $p$ , magnetic flux density  $\mathbf{B}$ , temperature  $T$  and the thermal energy density  $e$ . We assume a constant gravitational field  $\mathbf{g} = -g\hat{\mathbf{z}}$  within the domain. The viscous stress tensor  $\sigma$  is given by  $\sigma_{ij} = \nu\rho(\partial u_i/\partial x_j + \partial u_j/\partial x_i - 2/3\nabla \cdot \mathbf{u} \delta_{ij})$ .  $\nu$  denotes the kinematic viscosity and  $\chi$  the thermal conductivity coefficient. The values of  $\chi$ , the dynamic viscosity  $\nu_{\text{dyn}} = \nu\rho$  and the magnetic diffusivity  $\eta$  are constant over the box volume. An ideal gas equation of state is assumed with  $p = (\gamma - 1)e = k(m\bar{\mu})^{-1}\rho T$  where  $k$  is the Boltzmann constant,  $m$  the atomic mass unit,  $\bar{\mu}$  the mean molecular weight ( $\bar{\mu} = 1$  for all runs) and  $\gamma = C_p/C_V = 5/3$  is the ratio of the specific heats. The permeability  $\mu_0$  is given by the vacuum value  $\mu_0 = 4\pi \times 10^{-7} \text{VsA}^{-1}\text{m}^{-1}$ .

The equations (1)-(4) include more terms than usually appear in geodynamo simulations. Full compressibility is considered which means that sound-waves have to be resolved numerically and the density variation with height is retrieved in all terms in the equations (1)-(3). This is not a problem because “more” physics is included. In general geodynamo related simulations make use of the Boussinesq-Approximation,  $\nabla \cdot \mathbf{u} = 0$  (or  $\nabla \cdot \rho \mathbf{u} = 0$  in case of the anelastic approximation), where density is kept constant except for the buoyancy term  $\rho \mathbf{g}$  in the momentum equation (2), and sound-waves are filtered out. Physical processes on the time scale of sound waves are most probably not important for the geodynamo process and the Boussinesq (or anelastic approximation) should describe the properties in the Earth’s fluid outer core with sufficient accuracy but in connection with the  $\alpha$ -effect it is of interest to examine the meaning of the weak density stratification if compressibility acts as a symmetry breaker for the flow.

A disadvantage of our numerical approach is the very short time-step that is

determined by the sound-speed which is given by

$$c_s = \sqrt{\gamma \frac{k}{m\bar{\mu}} T}. \quad (5)$$

For the simulations presented in this paper the resulting Mach number  $\text{Ma} = u'/c_s$  is of the order of  $10^{-2}$  which is much larger than in the Earth's outer core (where  $\text{Ma}$  is of the order of  $10^{-7}$ ). Smaller Mach numbers in principle could be obtained by raising the sound-speed with respect to the turbulent motions. As a consequence the numerical time-step would become very small which would result in unacceptable long computation times if one performs the simulations for reasonable time periods to get sufficient statistics.

### 2.3 Initial state and input parameters

The simulations are started with an initial state that is given by a hydrostatic equilibrium and a polytropic temperature distribution in the absence of motions. This initial state is constructed such that a convective unstable density stratification is obtained, and the established convective state is only weakly dependent on the specific initial temperature- and density profiles (of course it depends on the values of  $\rho$  and  $T$  at the boundaries and the parameters that describe the molecular properties of the fluid).

From the equation of state and the condition for hydrostatic equilibrium,  $\partial_z p = -\rho g$ , together with the assumption of a polytropic temperature distribution,  $T = T_0 (\rho/\rho_0)^\Gamma$ , the initial density distribution can be calculated as

$$\rho(z) = \rho_0 \left( 1 + \frac{\partial_z T}{T_0} (d - z) \right)^{1/\Gamma}, \quad (6)$$

where  $d$  stands for the vertical box extension and the polytropic index  $\Gamma$  is given by  $\Gamma = \ln(1 + d\partial_z T/T_0) / \ln \xi$ . The stratification index  $\xi = \rho_{\text{bot}}/\rho_{\text{top}}$ , the temperature  $T_0$  and the global temperature gradient  $\partial_z T$  are prescribed input parameters whose values are given below. The subscript 0 refers to values taken at the top boundary of the box.

The gravitational acceleration can be calculated from the hydrostatic equilibrium condition and the initial density distribution (6) and is given by

$$g = \frac{\Gamma + 1}{\Gamma} \frac{k}{m\bar{\mu}} \partial_z T. \quad (7)$$

To obtain a convective unstable state the condition  $\Gamma > \gamma - 1$  must be fulfilled.

This is the case for our choice of the input parameters (see below) which results in  $\Gamma \approx 7.27$ .

All input quantities are measured at the top of the box. This is unproblematic because the density variation with depth is negligible and the temperature varies only by a factor of 2. The parameters  $\nu$ ,  $\chi$ ,  $\eta$  and  $\Omega$  are calculated from the Rayleigh number Ra,

$$\text{Ra} = \frac{\rho g C_p d^4}{\chi \nu} T \left( \partial_z T - \frac{g}{C_p} \right) \quad (8)$$

with  $C_p = k(m\bar{\mu})^{-1}\gamma(\gamma - 1)^{-1}$  the specific heat at constant pressure, Prandtl number  $\text{Pr} = \nu\rho C_p/\chi$ , magnetic Prandtl number  $\text{Pm} = \nu/\eta$  and Taylor number  $\text{Ta} = 4\Omega^2 d^4/\nu^2$ . The basic parameter set used for all simulations that are presented in this paper is given by  $\text{Ra} = 10^6$ ,  $\text{Pr} = 0.5$ ,  $\text{Pm} = 0.5$  and  $\text{Ta} = 10^7$ . The Elsässer number

$$\Lambda = \frac{\mathbf{B}^2}{2\Omega\mu_0\rho\eta} \quad (9)$$

serves as an input parameter for the magnitude of the imposed magnetic field whose influence is investigated by varying  $\Lambda$  from 0.01 to 100 covering the full range from weak fields to strong fields. The box with an aspect ratio 8:8:1 is placed at a latitude of  $\theta = 45^\circ$  on the northern hemisphere of the rotating spherical shell and a standard resolution of  $100 \times 100 \times 80$  grid points is used in all calculations. For all simulations temperature and density at the top of the box are scaled to unity, as it is the case for the global temperature gradient  $\partial_z T$  and the box height  $d$ . A stratification index of  $\xi = \rho_{\text{bot}}/\rho_{\text{top}} = 1.1$  is used.

#### 2.4 Boundary Conditions

All quantities are subject to periodic boundary conditions in the horizontal directions. At the top and at the bottom of the computational domain constant values for density and temperature are imposed. The vertical boundary condition for the magnetic field is a perfect conductor condition, and a stress-free boundary condition is adopted for the horizontal components of the velocity  $u_x$  and  $u_y$ . Impermeable box walls at the top and the bottom lead to a vanishing  $u_z$  at the vertical boundaries. Table 1 summarizes these conditions and gives the initial values for density and temperature which describe the overall stratification and the global temperature gradient.

Other boundary conditions for the magnetic field and the velocity have also been examined. Test calculations with rigid boundary conditions for the ve-

Table 1  
Vertical boundary conditions

	$\rho$	$T$	$\mathbf{u}$	$\mathbf{B}$
top	1	1	$\partial_z u_x = 0$	$\partial_z B_x = 0$
$(z = d)$			$\partial_z u_y = 0$	$\partial_z B_y = 0$
			$u_z = 0$	$B_z = 0$
bottom	1.1	2	$\partial_z u_x = 0$	$\partial_z B_x = 0$
$(z = 0)$			$\partial_z u_y = 0$	$\partial_z B_y = 0$
			$u_z = 0$	$B_z = 0$

locity lead to sharp Ekman layers at the vertical boundaries but only to small differences for the resulting EMF profiles. Slightly different boundary conditions for the magnetic field have been applied by Ziegler (2002) who used a divergence-maintaining linear extrapolation as the vertical boundary condition for the magnetic field. However, the same conditions used in the present simulations only lead to minor changes in field and flow behavior, and, in general, the profile of the EMF remains unchanged.

### 3 Results

#### 3.1 General properties

At first, a non-rotating non-magnetic convection model is computed and the resulting statistically steady state is used as initial condition for the full problem of rotating magnetoconvection. Typical values for the turbulent velocity  $\mathbf{u}'$  and the turbulent magnetic field  $\mathbf{B}'$  are obtained by an averaging procedure that includes the whole box volume. In the following, volume averages are indicated by double brackets,  $\langle\langle \cdot \rangle\rangle$ , whereas horizontal averages are denoted by single brackets,  $\langle \cdot \rangle$ . As root mean square value of fluctuations we define

$$\langle\langle f'^2 \rangle\rangle = (N_x N_y N_z)^{-1} \sum_{i,j,k} (f_{ijk} - \langle f \rangle_k)^2 \quad (10)$$

Here,  $N_x(N_y, N_z)$  denotes the number of grid cells in  $x, (y, z)$  direction and  $f_{ijk} - \langle f \rangle_k$  is the deviation of the fluctuating quantity at a certain grid cell labeled  $ijk$  from its horizontal average. Note that due to the horizontal averaging procedure and the periodic horizontal boundary conditions the mean quantities have no dependence on  $x$  or  $y$ .

Time averages are computed only over time intervals that show no significant change in the average itself. In the following, time is measured relative to the turnover time given by  $\tau_{\text{adv}} = d/u'$  where

$$u' = \sqrt{\overline{\langle\langle \mathbf{u}'^2 \rangle\rangle}} \quad (11)$$

and the overbar denotes time averaging. All time averages are calculated over a time range of at least  $20\tau_{\text{adv}}$  starting at a certain time after  $u'$  has reached a statistically steady state. A comparison with long-term computations shows that this is a sufficient time-span in order to obtain meaningful results.

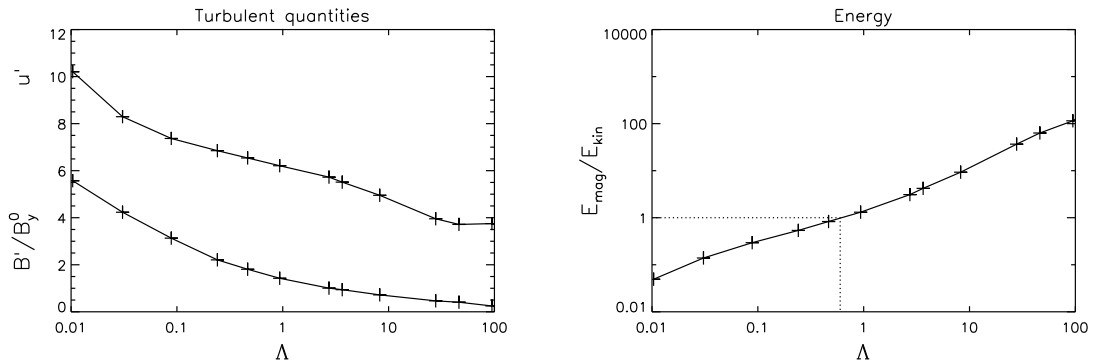


Fig. 2. Left: Quenching of turbulent velocity and (normalized) magnetic field fluctuations. Right: Ratio of the magnetic energy to the kinetic energy as a function of  $\Lambda$ .

The behavior of the turbulent velocity  $u'$  and the normalized turbulent magnetic field  $B'/B_y^0$  (where  $B'$  is defined analog to  $u'$ ) in dependence of the imposed magnetic field is shown in Figure 2 (left panel). Both quantities are significantly reduced compared to a non-magnetic but rotating convective state, reflecting the trend to a more laminar flow.

The ratio between the total magnetic energy and the kinetic energy is plotted in Figure 2 (right panel). Equipartition is reached for  $\Lambda \approx 0.6$  indicated by the dotted lines. For  $\Lambda > 0.6$  the magnetic energy clearly exceeds the kinetic energy. Increasing  $\Lambda$  from 0.01 to 100, the combined effects of rotation and the magnetic field lead to Rossby numbers  $\text{Ro} = u'/2\Omega d$  from  $7 \cdot 10^{-2}$  to  $3 \cdot 10^{-2}$  and turbulent Mach numbers  $\text{Ma} = u'/c_s$  from  $7 \cdot 10^{-2}$  to  $3 \cdot 10^{-2}$ . Reynolds numbers,  $\text{Re} = u'd/\nu$ , are in the range from  $\text{Re} = 210$  ( $\Lambda = 0.01$ ) to  $\text{Re} = 74$  ( $\Lambda = 100$ ).

### 3.2 Ohmic heating

The equation for the thermal or internal energy density (3) includes source terms for Ohmic heating and viscous heating. The volume integrals of the different contributions to the internal energy in relation to the overall internal energy  $E_{\text{int}} = \int e \, dV$  are plotted in Figure 3. Ohmic heating  $Q_{\text{Ohm}} = \int (\eta/\mu_0)(\nabla \times \mathbf{B})^2 \, dV$  (dashed-dotted line) is slightly larger than the viscous heating  $Q_{\text{vis}} = \int (\sigma \cdot \nabla \mathbf{u}) \, dV$  (thin solid line) which is a consequence of the relative large viscosity. More realistic parameters should significantly reduce the viscous heating compared to the Ohmic heating. Both terms are nearly constant in time. Heating by conductivity,  $Q_{\text{cond}} = \int \nabla \cdot (\chi \nabla T) \, dV$  (dashed line), shows stronger variations on a timescale of the turnover time and, on average, this term is of the same order than Ohmic- and viscous heating. All the three terms are balanced by cooling due to compressibility effects,  $Q_{\text{comp}} = -\int p \nabla \cdot \mathbf{u} \, dV$  (dotted line), which shows quite regular oscillations on the inertial timescale with a period  $P = \pi/(\Omega \cos \Theta) \approx 0.3\tau_{\text{adv}}$ . This balance is seen by the thick solid curve that gives the sum of all contributions. As a consequence, the internal energy of the box model remains nearly constant during all simulations.

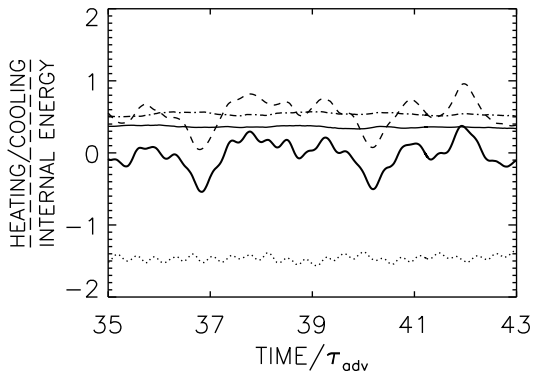


Fig. 3. Contributions to the internal energy balance scaled with the internal energy. The thin solid curve denotes viscous heating  $Q_{\text{vis}}$ , the dashed-dotted curve denotes the ohmic heating  $Q_{\text{Ohm}}$ , the dotted curve denotes cooling through compressibility  $Q_{\text{comp}}$  and the dashed curve denotes the conductivity term  $Q_{\text{cond}}$ . The sum of all contributions is shown by the thick solid curve.

Christensen and Tilgner (2004) retrieved a relation between the dissipation time  $\tau_{\text{diss}} = E_{\text{mag}}/Q_{\text{Ohm}}$  ( $E_{\text{mag}}$  the magnetic energy) and the dipole decay time  $\tau_{\text{dipol}} = R^2/(\pi^2\eta)$  which is given by  $\tau_{\text{diss}}/\tau_{\text{dipol}} = 1.74 \cdot \text{Rm}^{-1}$ . Although this result seems to be a quite general relation ( $\tau_{\text{diss}} \propto 1/u'$ ) it can only be confirmed for weaker magnetic fields. Figure 4 shows the dissipation time  $\tau_{\text{diss}}$  as it is defined above against the turbulent velocity  $u'$ . The dashed curve denotes a function proportional to  $1/u'$ . For  $u' > 6$  (corresponding to  $\Lambda < 1$ )

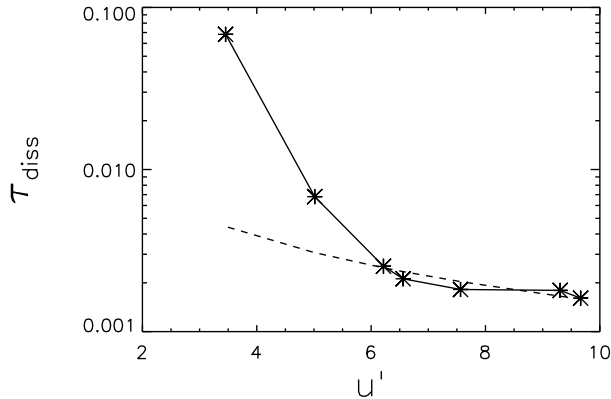


Fig. 4. Dissipation time against the turbulent velocity

this may be a reasonable approximation but for stronger imposed magnetic fields  $\tau_{\text{diss}}$  increases more strongly than it is described by the simple  $1/u'$ -law. The discrepancy most probably results from the two model settings – a self-consistent dynamo simulation in a spherical shell on the one hand and a local magnetoconvection simulation on the other. Especially the strong field case with  $\Lambda > 10$  can artificially be generated in a magnetoconvection simulation but in a dynamo simulation the nonlinear backreaction of the Lorentz force on the fluid flow probably leads to a saturation of the magnetic field at a lower magnitude, thus this part of the parameter space cannot be achieved in a dynamo simulation.

### 3.3 Patterns of flow and magnetic field

The dynamical influence of the imposed magnetic field can be seen in Figure 5 where the  $z$ -component of the velocity near the domain faces and in a horizontal plane at  $z = 0.5$  is shown. This plot shows a snapshot of the developed, rotating magnetoconvection for  $\Lambda \approx 1$  (left panel) and for  $\Lambda \approx 10$  (right panel). Upflows are visualized in grey whereas downflows are represented in dark tones. Compared to non-magnetic, rotating convection the magnetoconvection pattern remains nearly unchanged for  $\Lambda \lesssim 1$ . Many topologically unconnected columnar convection cells can be seen tilted by an angle of  $45^\circ$  with respect to the  $z$ -axis and become aligned with the rotation axis (Taylor-Proudman theorem).

Stronger magnetic fields lead to remarkable changes in the flow pattern. Between  $\Lambda = 1$  and  $\Lambda = 4$  the quasi-regular pattern becomes more and more disintegrated and evolves towards a nearly two-dimensional flow as illustrated in the right panel of Figure 5. The convection cells are clearly elongated along the imposed magnetic field direction ( $y$ -direction) and show little variations of the convective velocity along the field lines. The sheetlike convection cells are

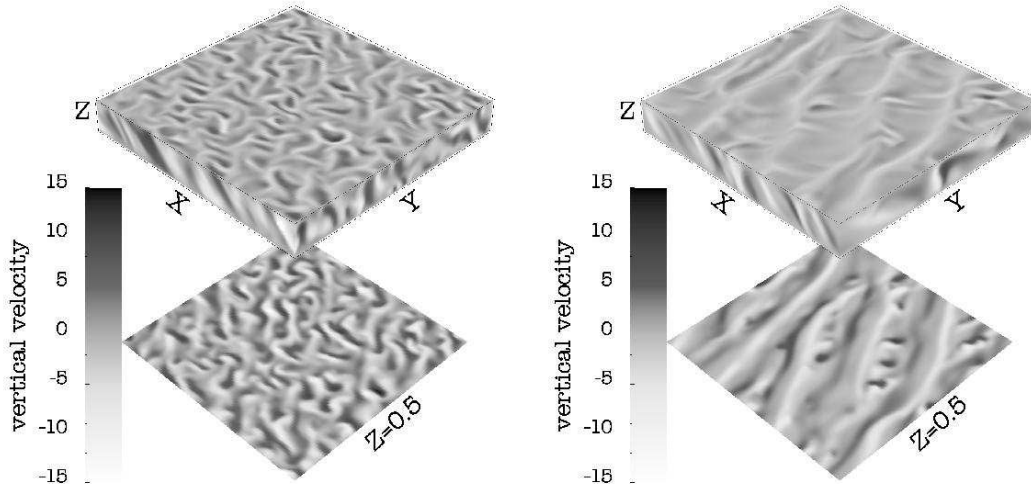


Fig. 5. Vertical velocity pattern of rotating magnetoconvection for  $\Lambda = 1$  (left) and  $\Lambda = 10$  (right).  $B_y$  is imposed.

again tilted inside the box and aligned with the rotation axis  $\boldsymbol{\Omega}$  as it is the case for the weak-field calculations. Compared to the cases of rotating convection or weak-field rotating magnetoconvection, the strong-field case is further characterized by a significant reduction of the number of convective cells. The nearly two-dimensionality of the flow can be explained from a condition similar to the Taylor-Proudman theorem for rotating spheres: For a stationary state with small deviations from the basic unperturbed state and neglecting diffusive terms it follows from the induction equation that  $B_i \partial_i u_j = 0$ , i.e. motions cannot vary in the direction of the imposed magnetic field (Chandrasekhar, 1961).

### 3.4 Mean fields

Figure 6 shows the components of the horizontally averaged magnetic field for a typical magnetoconvection simulation with  $\Lambda = 1$ . The top (bottom) row shows the  $z$ -profiles of the three components  $\langle B_x \rangle, \langle B_y \rangle, \langle B_z \rangle$  in case of an imposed field in  $x$  ( $y$ ) direction in units of the initial field  $B_0$ . The light gray lines represent different snapshots within the averaging period indicating substantial fluctuations, and the thick dashed line gives the time average of these individual curves.

A significant magnetic field component perpendicular to the initial imposed magnetic field exists close to the boundaries and there is a sign-change of this component in the center. In case of an imposed  $\langle B_x \rangle$  (Figure 6 upper row) the field component  $\langle B_y \rangle$  remains less than 10% of the initial field except near the vertical boundaries where  $\langle B_y \rangle$  becomes up to 40% of the initial imposed

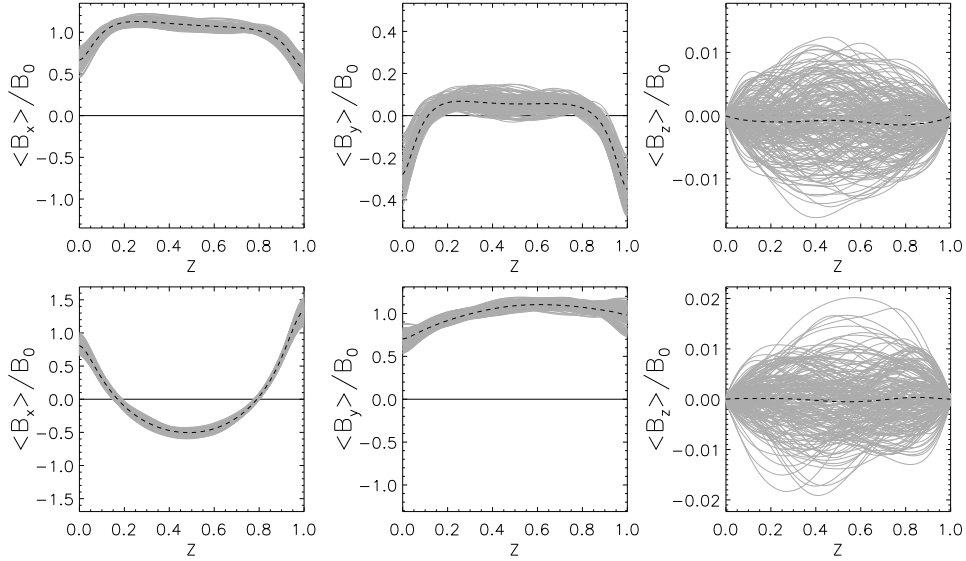


Fig. 6.  $z$ -dependence of the components of the mean magnetic fields for  $\Lambda = 1$ . Top row:  $B_x$  imposed, bottom row  $B_y$  imposed.  $\theta = 45^\circ$

field strength. This effect is larger in case of an initial imposed  $\langle B_y \rangle$  (Figure 6 lower row), where close to the boundaries the perpendicular component  $\langle B_x \rangle$  becomes as large as  $\langle B_y \rangle$  and up to 50% in the middle of the box.

The existence of a strong field component through the whole layer in the second case strongly differs from the results reported by Ziegler (2002) for highly stratified convection where the  $x$ -component of the magnetic field was found negligible ( $\langle B_x \rangle \ll \langle B_y \rangle$ ). This is probably due to a much lower Taylor number employed in the simulations of Ziegler (2002) and due to the initial two-layer configuration consisting of a convective unstable layer on top of a stable layer.

Since the induction equation for the mean magnetic field yields  $\partial_t \langle B_z \rangle = 0$  no  $\langle B_z \rangle$  can evolve during the simulations. Therefore, the magnetic energy in the vertical field component results from the fluctuating component  $B'_z$ . The above described structure of the  $z$ -profiles of the horizontal averaged field components is similar independent of the magnitude of the imposed magnetic field.

### 3.5 $\alpha$ -coefficients and kinetic helicity

Two separate runs are performed for each magnetic field strength where the magnetic field is imposed in the two perpendicular coordinate directions  $x$  and

$y$ . In general the EMF is given by

$$\mathcal{E}_i = \alpha_{ij} \langle B_j \rangle + \beta_{ijk} \frac{\partial \langle B_j \rangle}{\partial x_k}, \quad (12)$$

Under the assumption of isotropic turbulence  $\beta_{ijk} = \epsilon_{ijk} \eta_{\Gamma}$  (with  $\eta_{\Gamma}$  the turbulent diffusivity), the corresponding equations for the  $\alpha$ -coefficients are explicitly given by:

$$\mathcal{E}_x = \alpha_{xx} \langle B_x \rangle + \alpha_{xy} \langle B_y \rangle + \eta_{\Gamma} \frac{\partial \langle B_y \rangle}{\partial z}, \quad (13)$$

$$\mathcal{E}_y = \alpha_{yx} \langle B_x \rangle + \alpha_{yy} \langle B_y \rangle - \eta_{\Gamma} \frac{\partial \langle B_x \rangle}{\partial z}, \quad (14)$$

The results of a run with an imposed magnetic field in  $x$ -direction (in the following labeled by the superscript 1) are combined with the results from a run with an imposed magnetic field in  $y$ -direction (in the following labeled by the superscript 2). Then the equations (13) and (14) can be written in matrix form

$$\begin{pmatrix} \langle B_x^1 \rangle & \langle B_y^1 \rangle & 0 & 0 \\ 0 & 0 & \langle B_x^1 \rangle & \langle B_y^1 \rangle \\ \langle B_x^2 \rangle & \langle B_y^2 \rangle & 0 & 0 \\ 0 & 0 & \langle B_x^2 \rangle & \langle B_y^2 \rangle \end{pmatrix} \begin{pmatrix} \alpha_{xx} \\ \alpha_{xy} \\ \alpha_{yx} \\ \alpha_{yy} \end{pmatrix} = \begin{pmatrix} \mathcal{E}_x^1 - \eta_{\Gamma} \partial_z \langle B_y^1 \rangle \\ \mathcal{E}_y^1 + \eta_{\Gamma} \partial_z \langle B_x^1 \rangle \\ \mathcal{E}_x^2 - \eta_{\Gamma} \partial_z \langle B_y^2 \rangle \\ \mathcal{E}_y^2 + \eta_{\Gamma} \partial_z \langle B_x^2 \rangle \end{pmatrix}, \quad (15)$$

where we assumed that the  $\alpha$ -coefficients are independent from the direction of the imposed magnetic field.

In order to avoid problems due to the strong field gradients close to the boundaries we only use data with a  $z$  coordinate between  $z = 0.2$  and  $z = 0.8$ . Within this range the influence of the turbulent diffusivity is tested whereby  $\eta_{\Gamma}$  is estimated from the relation:

$$\eta_{\Gamma} = \frac{1}{3} \int_0^{\infty} \langle \mathbf{u}'(t) \mathbf{u}'(t - \tau) \rangle d\tau = \frac{1}{3} \langle \mathbf{u}'^2 \rangle \tau_{\text{corr}}. \quad (16)$$

The correlation time  $\tau_{\text{corr}}$  can be defined as the time  $\tau$  after which the correlation  $\langle \mathbf{u}'(t) \mathbf{u}'(t - \tau) \rangle$  at a time  $t$  is equal to  $1/e$  of the maximum value (given by  $\langle \mathbf{u}'^2(t) \rangle$ ). With that definition we derived

$$\tau_{\text{corr}} \approx 0.4 \dots 0.9 \tau_{\text{adv}} \quad (17)$$

which is then used to estimate  $\eta_T = 1/3 \cdot u^2 \tau_{\text{corr}}$ . This leads to a value of  $\eta_T$  which is approximately ten times larger than the molecular value of  $\eta$  as it is determined by the input parameters Ra, Pr and Pm. Equation (16) is the result of a quasi-linear calculation which is only valid under certain approximations and, therefore, this estimation of  $\eta_T$  should be treated with caution even if the result seems to be quite reasonable. To determine the importance of  $\eta_T$  we replaced  $\eta_T$  by  $\widetilde{\eta}_T = c_\eta \eta_T$  with a weighting factor  $c_\eta$  that was successively increased from 0 to 2. In all cases the influence of this term on the EMF and hence on the estimation of  $\alpha$  between  $z = 0.2$  and  $z = 0.8$  is not substantial. This is not surprising since the gradients of the mean magnetic field components in this interval are small. We thus neglect the terms involving  $\eta_T$  completely and solved system (15) by inverting the matrix and assuming that  $\eta_T \partial_z \langle B_{x,y}^{1,2} \rangle = 0$  on the right hand side of equation (15).

The results for the four considered elements of the  $\alpha$ -tensor,  $\alpha_{xx}$ ,  $\alpha_{xy}$ ,  $\alpha_{yx}$  and  $\alpha_{yy}$ , are shown in Figure 7 for three different (imposed) magnetic field strengths (from left to right:  $\Lambda = 0.1, 1, 10$ ).

We first discuss the non-diagonal elements  $\alpha_{xy}$  and  $\alpha_{yx}$ . The  $\alpha$ -tensor can be separated into a symmetric and antisymmetric part:

$$\alpha_{ij}^S = \frac{\alpha_{ij} + \alpha_{ji}}{2} \quad \alpha_{ij}^A = \frac{\alpha_{ij} - \alpha_{ji}}{2}. \quad (18)$$

In the mean-field induction equation the antisymmetric part corresponds to an advection term,  $\alpha^A \cdot \langle \mathbf{B} \rangle = \boldsymbol{\gamma} \times \langle \mathbf{B} \rangle$ , with  $\boldsymbol{\gamma} = -(\alpha_{yz}^A, \alpha_{zx}^A, \alpha_{xy}^A)$  (see e.g. Ossendrijver et al., 2002). The combination  $(\alpha_{xy} - \alpha_{yx})/2 \approx \alpha_{xy}$  plays the role of an advection in  $z$ -direction (radial direction in spherical coordinates). From Figure 7 we receive the approximate relationship  $\alpha_{xy} \approx -\alpha_{yx}$  thus  $\alpha_{xy}^S = 0$  which has been expected by theoretical reasons. The  $z$ -profile of  $\alpha_{xy}$  is – independently of  $\Lambda$  – predominantly positive. From that it follows that the advection velocity  $\gamma_z = -\alpha_{xy}$  is negative and the escape velocity in the vertical direction is directed downwards. Exactly this behavior has been obtained in a quasi-linear approximation by Kitchatinov and Rüdiger (1992) characterized as ‘turbulent buoyancy’. The same result has been found in numerical simulations by Dorch and Nordlund (2001), Ossendrijver et al. (2002) and Ziegler and Rüdiger (2003).

The diagonal components of the  $\alpha$ -tensor,  $\alpha_{xx}$  and  $\alpha_{yy}$  are responsible for dynamo action and, therefore, are of profound interest. We note that  $\alpha_{yy}$  shows a quite anti-symmetric behavior with respect to  $z$ . It is always negative in the lower part of the layer and positive in the upper part of the layer. The transition between negative and positive  $\alpha$ -effect occurs in the middle of the box leading to two extended zones with positive and negative  $\alpha$ -effect with nearly equal amplitude. The resulting vertical profiles of  $\alpha_{yy}$  differ from

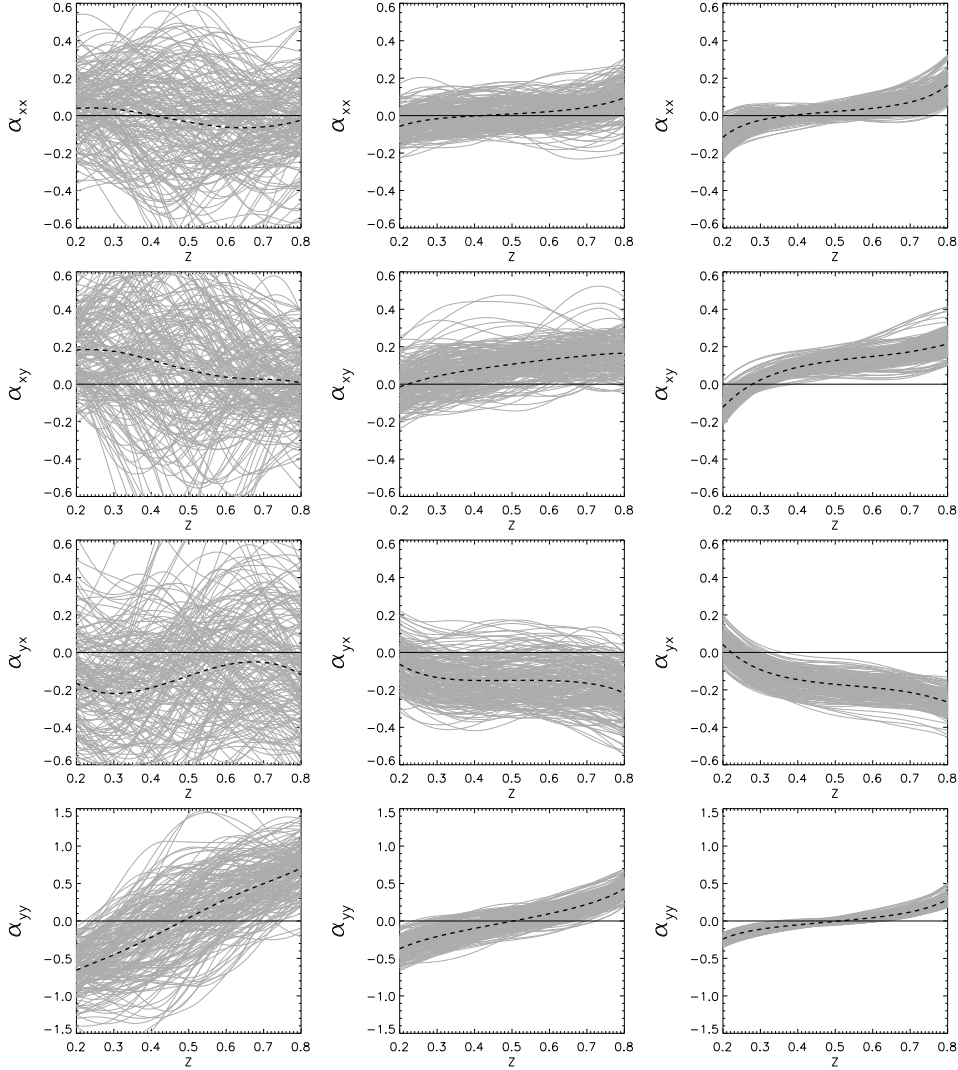


Fig. 7.  $z$ -dependence of  $\alpha$ -coefficients at  $\theta = 45^\circ$  for  $\Lambda = 0.1, 1, 10$  (from left to right). From top to bottom:  $\alpha_{xx}, \alpha_{xy}, \alpha_{yx}, \alpha_{yy}$

computations with stronger stratification where the  $z$ -dependence is much more asymmetric. In the latter scenario the zero line is crossed in the lower half-box and the magnitude of the  $\alpha$ -coefficients is larger in the upper half-box. This leads to a non-zero  $\alpha$ -effect when averaged over the entire box volume (Rüdiger and Hollerbach, 2004). In contrast to this, the volume averaged  $\alpha$ -effect is rather small in our model.

Between  $\Lambda = 0.1$  and  $\Lambda = 1$  the  $z$ -dependence of  $\alpha_{xx}$  undergoes a sign-change and the zero is below the middle of the box approximately at  $z \approx 1/3$ . In general the magnitude of  $\alpha_{xx}$  is clearly smaller than  $\alpha_{yy}$ . Figure 7 suggests that  $\alpha_{xx}$  slightly increases with the magnetic field strength but for stronger fields ( $\Lambda = 100$ ) both  $\alpha_{xx}$  and  $\alpha_{yy}$  vanish.

For increasing magnetic field time fluctuations in the  $\alpha$ -coefficients are obviously reduced which comes from the fact that the flow tends to become laminar for large  $\Lambda$ .

Comparing the  $\alpha_{yy}$ -profiles with the corresponding kinetic helicity shown in Figure 8 the well-known relation between the signs of the  $\alpha$ -coefficient and the kinetic helicity is confirmed, i.e.

$$\alpha \approx -\frac{1}{3}\tau_{\text{corr}} \langle \mathbf{u}' \cdot \nabla \times \mathbf{u}' \rangle \quad (19)$$

with a correlation time  $\tau_{\text{corr}}$  (see e.g. Krause and Rädler, 1980). A similar relation was found by Ossendrijver et al. (2001).

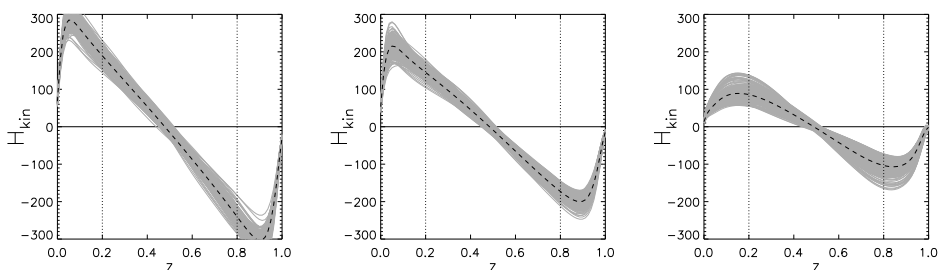


Fig. 8.  $z$ -dependence of the kinetic helicity  $H_{\text{kin}} = \langle \mathbf{u}' \cdot \nabla \times \mathbf{u}' \rangle$  at  $\theta = 45^\circ$  for  $\Lambda = 0.1, 1, 10$  (from left to right). The vertical lines denote the  $z$ -range that has been used to calculate  $\alpha$ .

Increasing the strength of the imposed magnetic field the change in amplitude of the helicity is roughly in accordance with the change in amplitude of  $\alpha_{yy}$ . For imposed magnetic fields with  $\Lambda \lesssim 10$  the correlation time  $\tau_{\text{corr}}$  defined by equation (19) is of the order of 10% of the turnover time  $\tau_{\text{adv}}$ . This estimation is smaller than the correlation time that has been calculated from equation (16), most probably because the connection between helicity and  $\alpha$ -effect from equation (19) is only a very rough estimation that rather describes the relation between the signs of  $\alpha$  and helicity.

### 3.6 $\alpha$ -quenching

In order to estimate the quenching behavior of the  $\alpha$ -effect we investigate the variation of  $\alpha_{yy}$  in dependence of  $\Lambda$ . The quenching curve is plotted in Figure 9 where the solid (dashed) line corresponds to the volume averaged  $\alpha_{yy}$  in the lower (upper) part of the box where  $\alpha_{yy}$  is negative (positive). The dotted line shows a simple analytic quenching function of the form

$$\alpha(B) = \alpha(B \rightarrow 0) \cdot \frac{1}{1 + (B_y^0/B_{\text{eq}})^3}. \quad (20)$$

where  $B_y^0$  denotes the initially imposed magnetic field strength and  $B_{\text{eq}}$  is the so called equipartition field which is defined by  $B_{\text{eq}}^2 = \mu_o \rho u'^2 (B \rightarrow 0)$ , i.e.  $u'$  is related to the non-magnetic case. A value of  $B_y^0/B_{\text{eq}} = 1$  (equipartition value) corresponds to  $\Lambda \approx 6.2$ .

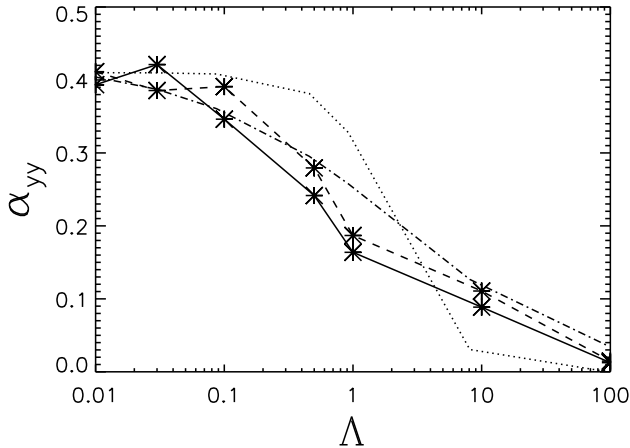


Fig. 9. Quenching behavior of  $\alpha_{yy}$ . The solid (dashed) line corresponds to the average  $\alpha_{yy}$  in the lower (upper) half of the box. The dotted line shows the analytic quenching function (20).

The  $\alpha$ -effect is quenched under the influence of strong external magnetic fields but the suppression is not catastrophic. The quenching behavior described by the analytic function (20) is underestimated between  $\Lambda \approx 0.1$  and  $\Lambda \approx 4$ , and it is overestimated for  $\Lambda > 10$ , but in general (20) reproduces the data quite well. Independent of  $\Lambda$  the averaged absolute value of  $\alpha_{yy}$  in the upper half of the box is roughly 10% larger than in the lower half of the box which most probably is the result of the small available density stratification.

## 4 Conclusions

The main result of our simulations is that the  $\alpha$ -effect describing the production of poloidal field from toroidal field (characterized by  $\alpha_{yy}$ ) is positive in the upper half of the box and negative in the lower half of the box. Symmetry breaking through compressibility only has a weak influence on the solution. The zero of the  $\alpha$ -effect is located in the middle of the box and the magnitude of the  $\alpha$ -effect in the upper half of the box is only slightly larger than in the lower half. In all cases the  $\alpha$ -effect should vanish at the top and at the bottom of the box because of the boundary conditions. The form of the  $\alpha$ -profile and the connection of the  $\alpha$ -effect with the kinetic helicity suggest that the maximum of the  $\alpha$ -effect is located inside the boundary layers that have not been considered because close to the vertical boundaries the established

configuration of the magnetoconvection state does not allow to estimate the  $\alpha$ -coefficients without contradiction. A good approximation to these properties of the  $\alpha$ -effect are solutions proportional to  $\sin(2\pi z)$  that have been found from quasi-linear calculations by Soward (1974).

An estimation of the strength of the  $\alpha$ -effect is given by the dynamo number  $C_\alpha = \alpha d / \eta_T$ . The results from the simulations can be scaled:

$$\alpha_E = \alpha_s \frac{u'_E}{u'_s} \quad \eta_{T,E} = \eta_{T,s} \frac{\eta_E}{\eta_s}, \quad (21)$$

where the subscript E denotes Earth values (typical:  $u'_E = 5 \cdot 10^{-4} \text{m/s}$  and  $\eta_E = 2 \text{m}^2/\text{s}$ ). The subscript s denotes results from the presented simulations. For moderate  $\Lambda$  typical values are  $\alpha_s / u'_s \approx 0.1$  and  $\eta_{T,s} / \eta_s \approx 10$ . Taken  $d_E \approx 2000 \text{km}$  as the thickness of the fluid outer core this leads to  $C_\alpha \approx 5$ . This may be large enough to ensure dynamo action in a mean-field model, but this calculation of  $C_\alpha$  is rather uncertain. Especially  $\eta_T$  is only roughly estimated, and it is doubtful if the simple scaling law (21) is suitable to extrapolate the correct values of  $\alpha$  and  $\eta_T$  for the Earth case.

With the present work it cannot be ruled out that the  $\alpha$ -effect is larger for more suitable parameters, e.g. faster rotation or higher Rm. Indeed, Ossendrijver et al. (2001) showed that the horizontal  $\alpha$ -effect at the north pole ( $\alpha_H = \alpha_{xx} = \alpha_{yy}$  because x and y are indistinguishable at  $\theta = 0^\circ$ ) increases with rotation, whereas the vertically  $\alpha$ -effect ( $\alpha_V = \alpha_{zz}$ ) is quenched for faster rotation. Computations with stronger driven convection and faster rotation would be necessary to investigate for more reliable scaling laws like (21) of the  $\alpha$ -effect and to examine if a stronger driven turbulence would result in a larger  $\alpha$ -effect. Finally a comparison of  $\alpha$  (respective the electromotive force  $\mathcal{E}$ ) from global geodynamo simulations where  $\mathbf{B}$  is produced by self-consistent dynamo-action with the results presented in this work would be of interest to find out if there exists common properties e.g. a connection with the kinetic helicity.

## Acknowledgements

This work was supported by the DFG SPP 1097 ‘‘Erdmagnetische Variationen: Raum-Zeitliche Struktur, Prozesse und Wirkungen auf das System Erde’’.

## References

- Buffett, B. A., 2003. A comparison of subgrid-scale models for large-eddy simulations of convection in the Earth's core. *Geophysical Journal International* 153, 753–765.
- Busse, F. H., 1970. Thermal instabilities in rapidly rotating systems. *Journal of Fluid Mechanics* 44, 441–460.
- Chandrasekhar, S., 1961. *Hydrodynamic and hydromagnetic stability*. International Series of Monographs on Physics, Oxford: Clarendon.
- Christensen, U., Tilgner, A., 2004. Power requirement of the geodynamo from ohmic losses in numerical and laboratory dynamos. *Nature* 429, 169–171.
- Dorch, S. B. F., Nordlund, Å., 2001. On the transport of magnetic fields by solar-like stratified convection. *A&A* 365, 562–570.
- Hollerbach, R., 1996. On the theory of the geodynamo. *Phys. Earth Planet. Inter.* 98, 163–185.
- Hollerbach, R., 2003. The range of timescales on which the geodynamo operates. *Geodynamics Series* 31, 181–192.
- Kitchatinov, L. L., Rüdiger, G., 1992. Magnetic-field advection in inhomogeneous turbulence. *A&A* 260, 494–498.
- Krause, F., Rädler, K. H., 1980. *Mean-field magnetohydrodynamics and dynamo theory*. Oxford: Pergamon Press.
- Olson, P., Christensen, U., Glatzmaier, G. A., 1999. Numerical modeling of the geodynamo: Mechanisms of field generation and equilibration. *Jour. Geophys. Res.* 104, 10383–10404.
- Ossendrijver, M., Stix, M., Brandenburg, A., 2001. Magnetoconvection and dynamo coefficients: Dependence of the alpha effect on rotation and magnetic field. *A&A* 376, 713–726.
- Ossendrijver, M., Stix, M., Brandenburg, A., Rüdiger, G., 2002. Magnetoconvection and dynamo coefficients. II. Field-direction dependent pumping of magnetic field. *A&A* 394, 735–745.
- Roberts, P. H., Glatzmaier, G. A., 2000. Geodynamo theory and simulations. *Reviews of Modern Physics* 72, 1081–1123.
- Rüdiger, G., Hollerbach, R., 2004. *The Magnetic Universe - Geophysical and Astrophysical Dynamo Theory*. Wiley-VCH Verlag Berlin.
- Schmitt, D., Ossendrijver, M. A. J. H., Hoyng, P., Oct. 2001. Magnetic field reversals and secular variation in a bistable geodynamo model. *Physics of the Earth and Planetary Interiors* 125, 119–124.
- Soward, A. M., 1974. A Convection-Driven Dynamo. I. The Weak Field Case. *Royal Society of London Philosophical Transactions Series A* 275, 611–646.
- Stefani, F., Gerbeth, G., 2003. Oscillatory mean-field dynamos with a spherically symmetric, isotropic helical turbulence parameter  $\alpha$ . *Physical Review E* 67, 027302.
- Stefani, F., Gerbeth, G., 2004. Asymmetric polarity reversals, bimodal field distribution, and coherence resonance in a spherically symmetric mean-field dynamo model. *subm.*

- Ziegler, U., 1998. NIRVANA+: An adaptive mesh code for compressible MHD. *Comp. Phys. Comm.* 109, 111.
- Ziegler, U., 1999. A Cartesian adaptive mesh code for compressible MHD. *Comp. Phys. Comm.* 116, 65.
- Ziegler, U., 2002. Box simulations of rotating magnetoconvection. Spatiotemporal evolution. *A&A* 386, 331–346.
- Ziegler, U., Rüdiger, G., 2003. Box simulations of rotating magnetoconvection. Effects of penetration and turbulent pumping. *A&A* 401, 433–442.